



**HAL**  
open science

# Oceanic Kelvin waves and tropical Atlantic intraseasonal variability: 1. Kelvin wave characterization

Irene Polo, Alban Lazar, Belén Rodríguez-Fonseca, Sabine Arnault

## ► To cite this version:

Irene Polo, Alban Lazar, Belén Rodríguez-Fonseca, Sabine Arnault. Oceanic Kelvin waves and tropical Atlantic intraseasonal variability: 1. Kelvin wave characterization. *Journal of Geophysical Research*, 2008, 113, pp.07009. 10.1029/2007JC004495 . hal-00770610

**HAL Id: hal-00770610**

**<https://hal.science/hal-00770610>**

Submitted on 22 Nov 2021

**HAL** is a multi-disciplinary open access archive for the deposit and dissemination of scientific research documents, whether they are published or not. The documents may come from teaching and research institutions in France or abroad, or from public or private research centers.

L'archive ouverte pluridisciplinaire **HAL**, est destinée au dépôt et à la diffusion de documents scientifiques de niveau recherche, publiés ou non, émanant des établissements d'enseignement et de recherche français ou étrangers, des laboratoires publics ou privés.

Copyright

# Oceanic Kelvin waves and tropical Atlantic intraseasonal variability:

## 1. Kelvin wave characterization

Irene Polo,<sup>1</sup> Alban Lazar,<sup>2</sup> Belen Rodriguez-Fonseca,<sup>1</sup> and Sabine Arnault<sup>2</sup>

Received 9 August 2007; revised 11 March 2008; accepted 27 March 2008; published 8 July 2008.

[1] Oceanic Kelvin waves from the equator to the West African coast are investigated in the framework of tropical Atlantic intraseasonal variability. In order to better highlight the wave propagations, a 25–95 day band-pass filter was applied to the sea surface height (SSH) product derived from the TOPEX/POSEIDON altimeter and an ocean general circulation model simulation for the 1993–2000 period. In addition to equatorial eastward propagations, our analysis reveals recurrent and continuous propagations distinguishable over thousands of kilometers poleward along the coasts as far as about 10°–15° latitude, a novel result with altimeter data. The variance of the filtered SSH signal goes from 1 cm at the equator to 2 cm at the African coast. Estimates of the phase speed range from 1.5 to 2.1 m/s along the equator and the West African coastline. Such values are very close to those of equatorial Kelvin wave propagations, likely dominated by the first two baroclinic modes, supporting the fact that the coastal propagations are coastally trapped Kelvin waves. In order to simplify the description of these Kelvin waves, we present an intraseasonal climatology which reveals regular boreal autumn–winter equator to coast propagations. An improved description is achieved thanks to the computation of an extended empirical orthogonal function for the boreal autumn–winter propagations. Lag correlation of SSH signals allows for a twofold quantification: the phase speed and the importance of remote forcing along the coast. The remote forcing effect of intraseasonal Kelvin waves is clearly evidenced over coastal upwelling regions as far as 10°–15° latitude. The physical mechanism associated with the forcing of the Kelvin waves and its impacts will be investigated in a future paper.

**Citation:** Polo, I., A. Lazar, B. Rodriguez-Fonseca, and S. Arnault (2008), Oceanic Kelvin waves and tropical Atlantic intraseasonal variability: 1. Kelvin wave characterization, *J. Geophys. Res.*, *113*, C07009, doi:10.1029/2007JC004495.

### 1. Introduction

[2] Most of the heat content variability in the tropical ocean is located in the upper layer; as a result, low-latitude oceans are often approximated as a two-layer system. This attribute approximation implies that variations in the depth of the thermocline, and hence of the heat content, are directly reflected in sea surface height (SSH) [Rebert *et al.*, 1985], with the first baroclinic mode being dominant.

[3] As shown by Matsuno [1966] and Moore [1968], the latitude band of the tropical oceans is the site of a singular set of equatorial waves that propagate eastward (equatorial Kelvin waves) or westward (Rossby waves). Their sea level signature is adequate to their detection, and satellite altimeters can measure the signals down to a few centimeters. Although altimeter measurements primarily reflect the movement of the thermocline, because of the near-surface intensification of baroclinic modes [Stammer, 1997], second and third baroclinic modes could also be important in the

actual tropical Atlantic (TA) [Du Penhoat and Treguier, 1985; Illig *et al.*, 2004; Schouten *et al.*, 2005]. The phase speed estimated of the equatorial Atlantic is 2.6 m/s for the first vertical mode Kelvin wave and 1.4 and 0.8 m/s for the second and third vertical modes [Schouten *et al.*, 2005; Illig *et al.*, 2004].

[4] The TA dynamic sea level variability is dominated by the seasonal cycle [Arnault and Cheney, 1994]. The seasonal adjustment of the ocean to the forcing of the wind stress causes a cycle of consecutive Rossby and Kelvin waves. Figure 1a shows the seasonal cycle of the sea level and the wind stress along the equator and the West African coast. Figure 1a (similar to the one shown by Schouten *et al.* [2005] and Rouault *et al.* [2007]), computed here as the sum of the annual and semiannual harmonics, is characterized by an upwelling season (May to October) and a downwelling season (November to April) at the eastern equator, coinciding with the strengthening and weakening of the trade winds at the equator. Along the coast of the Gulf of Guinea (GG), coinciding with the two upwelling seasons (February–March and August–September [Picaut, 1983]), there are some apparent coastal propagations of the sea level (February–March and August–September in Figure 1a, left) which are slower than the one expected from theoretical

<sup>1</sup>Departamento de Geofísica y Meteorología, Facultad de C.C. Físicas, Universidad Complutense Madrid, Madrid, Spain.

<sup>2</sup>LOCEAN-IPSL, University of Paris VI, Paris, France.

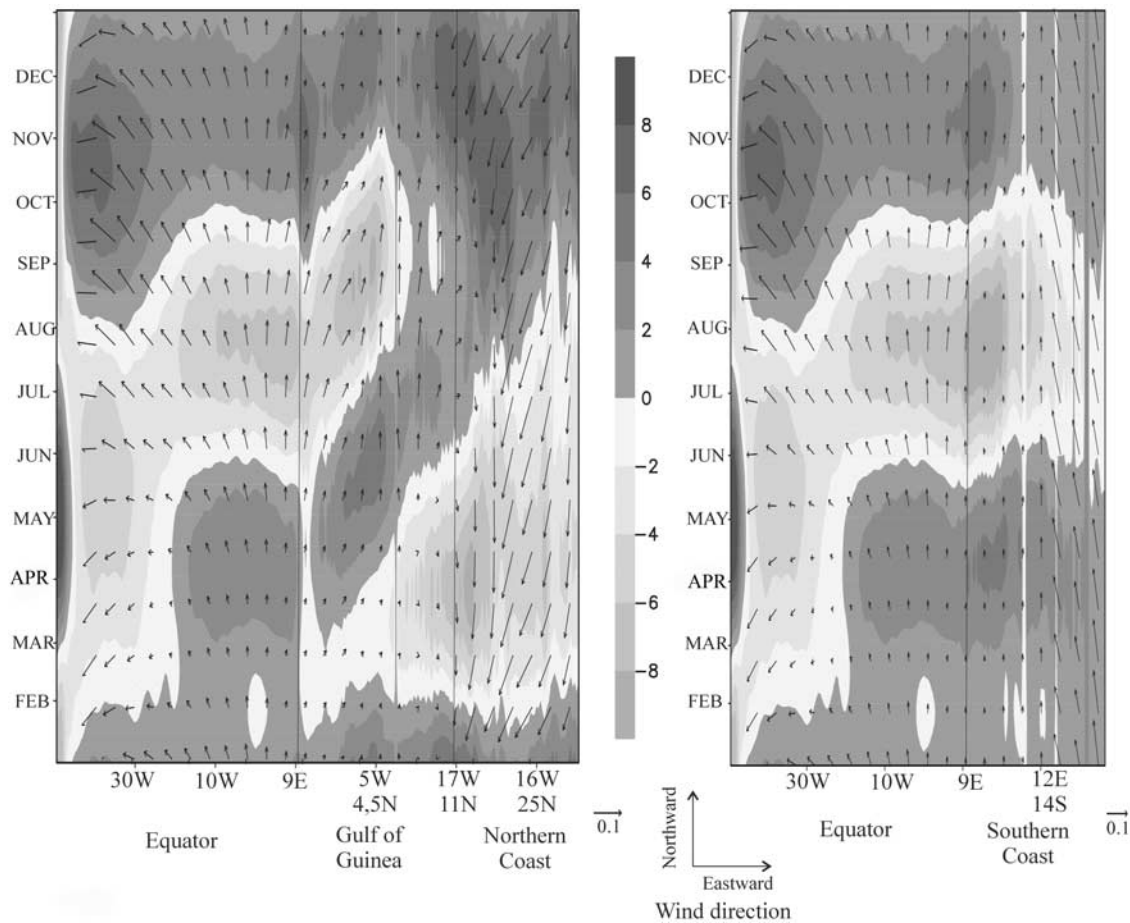


**Figure 1a.** Seasonal cycle of the observed T/P SSH (shaded areas in cm) and the wind stress (vectors in  $10^{-1} \text{ N/m}^2$ ) for the equatorial Atlantic and the (left) northern and (right) southern African coast. The wind stress is projected positively eastward and northward over virtual  $x$  and  $y$  axes, respectively.

first-mode Kelvin wave propagations [Schouten *et al.*, 2005] and whose wave nature is not clear. One might wonder from Figure 1a whether there are only high-order slow modes along the coast or if the lowest-order baroclinic modes are masked by wind changes associated with the Intertropical Convergence Zone (ITCZ) migration or other large-scale processes. In order to answer this question, an additional processing of the signal is thus necessary to verify the latter mentioned coastal propagations.

[5] Since Matsuno [1966] established the equations of the shallow water equatorial waves, several early studies advocated the idea that part of the equatorial and coastal upwelling in the GG is remotely forced by the wind in the western equatorial Atlantic via Kelvin waves [Moore *et al.*, 1978; Adamec and O'Brien, 1978; O'Brien *et al.*, 1978; Clarke, 1979; Servain *et al.*, 1982]. Further elements were presented in support of coastal wave propagation in the TA with sea surface temperature (SST) [Picaut, 1983] and tide gauges records [Aman *et al.*, 2007]. A new stage started when TOPEX/POSEIDON (T/P) was launched in 1992, and since then, Kelvin wave propagations have been better described in the equatorial Atlantic [Katz, 1997; França *et al.*, 2003; Illig *et al.*, 2004; Schouten *et al.*, 2005; Han *et al.*, 2008] and equatorial Pacific [Kessler *et al.*, 1995; Meyers *et al.*,

1998; Cravatte *et al.*, 2003; Roundy and Kiladis, 2006]. These studies used band-pass filters in order to avoid the masking effect of large-scale signals, and this is also the strategy we adopted in this paper.

[6] Regarding theoretical studies about the continuity of the equatorial Kelvin waves along the eastern boundary, Moore [1968] established that the equatorial Kelvin waves could be reflected in the eastern boundary and, in part, could propagate poleward as coastally trapped waves. Although Clarke [1983] also analytically established the equatorial wave reflection in an oceanic boundary, he found that the reflection occurred without dissipation. Greatbatch and Peterson [1996] described how the stratification changes could slow down the coastally trapped wave propagation in high latitudes. Using observational data, convincing elements have been presented for Kelvin wave propagations from the equator to the coast in the eastern Pacific at intraseasonal [Hormazabal *et al.*, 2002] and interannual time scales, especially during El Niño–Southern Oscillation (ENSO) events [Jacobs *et al.*, 1994; Meyers *et al.*, 1998; Vega *et al.*, 2003]. Grodsky and Carton [2006] have found coherent interannual variations of SSH in the equatorial Atlantic and the southern subtropical Atlantic. They hypothesized that a link between the two is provided by

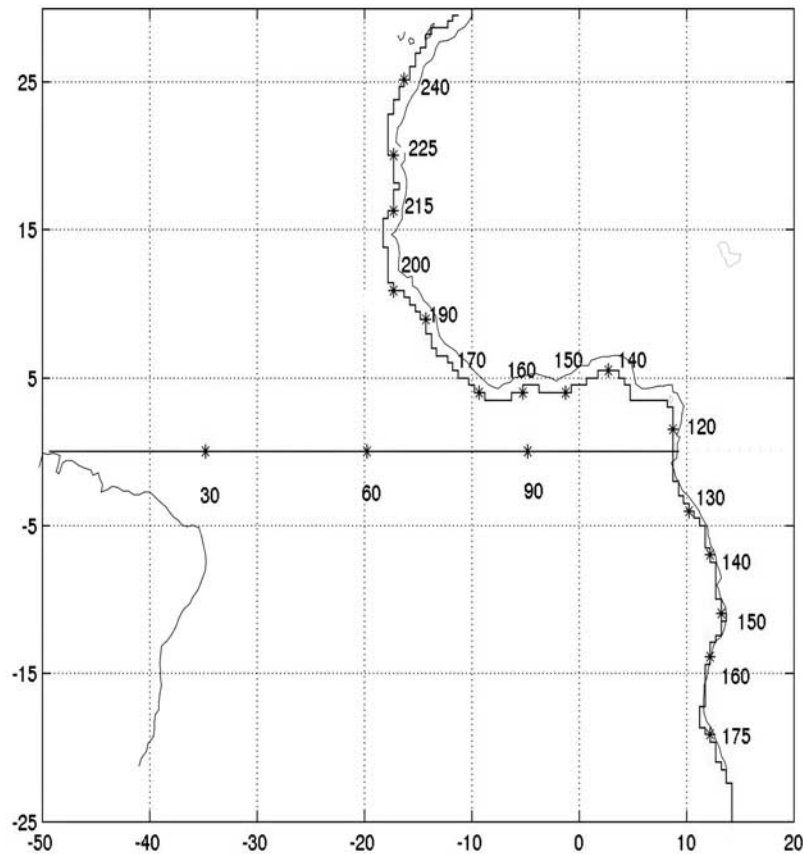


**Figure 1b.** Map of the grid points along the equator and the African coast used in the study of Kelvin wave tracks.

coastal waves propagating southward along the African coast.

[7] Along the coast, one way of dissipation of the Kelvin wave energy is the radiation of Rossby waves from the eastern boundary [Gill, 1982]. The Rossby wave, when reaching the western boundary, can then potentially trigger a new Kelvin wave at the western equator. However, *Arnault et al.* [1990], *Handoh and Bigg* [2000], and *Illig et al.* [2004] have argued that the small Atlantic basin and the presence of the North Brazil Current (NBC) could inhibit the Rossby reflection. They have experienced difficulties backtracking equatorial waves up to the American coast.

[8] In this paper, we have focused our analysis on intraseasonal time scales. At these scales, the Kelvin wave activity has been pointed out, mainly in the Pacific basin, to be associated with the convection activity, which can be important in climate terms [Kessler et al., 1995; Hendon et al., 1998; Roundy and Kiladis, 2006]. In the TA, intraseasonal variability modulates the main annual to interannual basin signals of important processes (i.e., West African Monsoon, oceanic cold tongue over the eastern equatorial Atlantic, seasonal coastal upwelling at the West African coast). Therefore, it is important to investigate the nature of the intraseasonal SSH signal and, in particular, its contribution to the teleconnection processes within the tropics. Furthermore, an unambiguous detection of continuous

propagating signals from the equator to the subtropical along the eastern Atlantic Ocean coastlines at intraseasonal scales is still missing, and we understand there is a need of filling this gap through further investigation. It is the goal of this paper to provide a sound description of this phenomenon over the TOPEX/POSEIDON 1993–2000 time period using the satellite measurements combined with an ocean general circulation model (OGCM) simulation. In a future paper (hereinafter referred to as paper 2), we will analyze the various forcing of these waves as well as some of its impacts in relation to the TA intraseasonal variability. This paper presents a detailed description of the data used (section 2). After a discussion of the choice of the band-pass filter (section 4), we study the intraseasonal propagating SSH anomalies in the observations and the OGCM (section 5) through a climatology and, focusing on boreal autumn–winter season, the main propagating mode. Then apparent propagation phase speeds are quantified, and the remote impacts are characterized (section 6). Finally, the main conclusions are summarized.

## 2. Description of the Data

[9] We use SSH TOPEX/POSEIDON altimetry measurements with  $0.5^\circ$  horizontal resolution and 7 day time resolution produced and distributed by Aviso, as part of

the Ssalto ground processing segment. The T/P SSH anomalies have already been corrected by removing 4 year average elevation and signals such as the ocean tide, the dry tropospheric, inverted barometer, tidal aliasing, and vapor water. The intercomparison analyses with in situ measurements (i.e., tide gauges records) have demonstrated that the altimetry is an important tool to observe oceanic variability [Arnault *et al.*, 1992], even in the coastal regions [Aman *et al.*, 2007]. In contrast to the sparse network of coastal tide gauges, measurements of SSH from space by satellite radar altimetry provide near-global and homogeneous coverage of the world's oceans. The weekly temporal resolution of the T/P SSH is expected to be high enough for the description of the baroclinic Kelvin waves since the theoretical first baroclinic mode takes about 30–45 days to cross the Atlantic along the equator and more than 20 days to leave the tropical latitudes studied here. However, the  $0.5^\circ$  spatial resolution corresponds to the Rossby radius of deformation at about  $15^\circ$  latitude for a 2 m/s baroclinic phase speed. Therefore, it is certainly a limitation to our analysis, and it may, in particular, affect our ability to observe coastal waves poleward of  $10^\circ$ – $20^\circ$  latitude (see Figure S1 in the auxiliary material.<sup>1</sup>)

[10] In order to complete the study with synchronous subsurface oceanic quantities that are not available in the observations, in particular the thermocline depth, we use a numerical simulation of the Océan Parallélisé (OPA) OGCM [Madec *et al.*, 1998]. The ORCA05 configuration used here was run at the Laboratoire d'Océanographie et du Climat: Expérimentations et Approches Numériques (LOCEAN) laboratory by the Numerical Framework for Ocean Modeling (NEMO) team for the 1992–2000 period. The configuration is for the global ocean with a  $0.5^\circ$  horizontal resolution and 30 vertical levels. The momentum flux is the weekly ERS-1 and -2 wind stress interpolated daily, while the air-sea heat fluxes are computed in line with semiempirical, or bulk, formulas using OGCM SST, the ERS-1 and -2 wind speed, the NCEP-NCAR reanalysis [Kalnay *et al.*, 1996] air temperature, and monthly climatological air humidity [Trenberth *et al.*, 1989] and cloudiness [Berliand and Strokina, 1980]. Precipitation data come from the Climate Prediction Center Merged Analysis of Precipitation (CMAP) product [Xie and Arkin, 1996]. Major river runoffs are taken into account through monthly values of river discharge [UNESCO, 1996]. At last, a restoring term toward Levitus [1998] sea surface salinity is applied to the freshwater budget. For further details on the model configuration, see de Boyer Montégut *et al.* [2007].

[11] In this work we have used 5 day average output of SSH and  $18^\circ\text{C}$  isotherm depth (hereinafter referred to as z18). We have chosen the  $18^\circ\text{C}$  isotherm depth as the thermocline depth proxy after having analyzed the isotherms ranging from  $15^\circ\text{C}$  to  $25^\circ\text{C}$ . The  $18^\circ\text{C}$  isotherm depth appears to be the most representative thermocline proxy over the African coastlines, in particular, within upwelling areas where the isotherms outcrop. Note that the pycnocline (represented as sigma-26 isopycnal depth  $\sigma_{26}$ ) is theoretically more closely related to waves and it has more physical meaning than z18. However, z18 is much

better geographically defined than  $\sigma_{26}$ , especially in the coastal areas; therefore, z18 will be used in this study. In section 3, some basic statistics are performed to show the ability of the model to reproduce the SSH observations for the 1993–2000 period.

[12] To follow the Kelvin wave propagation, wave tracks have been defined along the equator and the African coast following the model grid; thus, the distance between two grid points is  $0.5^\circ$  ( $\sim 55$  km). For the sake of minimizing data gaps, the northern coastal track points have been shifted  $0.5^\circ$  offshore. The corresponding wave tracks are shown in Figure 1b along the equator and poleward along the African coast. To the north, the track moves westward along the GG and continues northward up to  $30^\circ\text{N}$ , having 2 times more track points than the south. To the south, the track runs up to  $25^\circ\text{S}$  along the coast (hereinafter referred to as the southern African coast). Note that both north and south wave tracks share the first  $\sim 120$  points corresponding to the equatorial Atlantic. It bears mentioning that following the coastline along different isobaths (0, 200, 400, 1000 m) does not make substantial differences and no remarkable properties changes are found (not shown). In this paper, generally, for the sake of simplicity, the term “Kelvin wave” refers to the equatorial and coastally trapped propagations, even though the coastal wave nature may be a mix of Kelvin and topographic waves.

### 3. Interannual SSH Anomalies

[13] The annual and semiannual components dominate the sea level variability over the equator and the African coast [Wilson and Adamec, 2002; Schouten *et al.*, 2005; Aman *et al.*, 2007]. Figure 2 shows Hovmuller diagrams of the observed SSH interannual anomalies along the wave tracks, which are the result of removing the seasonal cycle relative to the above mentioned harmonics to the total signal. The result of this truncation (Figure 1a) is similar to the one obtained when performing the seasonal cycle with higher truncation or with a simple climatological average (see Figure S2 in the auxiliary material). Although propagations are difficult to identify unequivocally because of basin-scale interannual SSH anomalies [Handoh and Bigg, 2000; França *et al.*, 2003], many propagating-like signals appear strikingly going from the equator to the African coast along the GG (Figure 2, left) and along the southern African coast (Figure 2, right). It is also noticeable that some points are particularly noisy: in the western equator (equatorial track points 0–20), at  $5^\circ\text{S}$  (south track point 140), and at  $10^\circ\text{N}$  (north track point 200). The first two locations correspond to the Amazon and the Congo River runoff, whereas the last location corresponds to the large offshore extension of the continental plateau, likely associated with strong tidal signals.

[14] Figure 2 shows extreme positive and negative events associated with the 1995–1996, 1998, and 1999 warm events and the 1994, 1997, and 2000 cold events. Some of those years have been described by other authors in relation to a self-sustaining Atlantic climate mode [Handoh and Bigg, 2000], to interannual variability modes [Sutton *et al.*, 2000; Illig *et al.*, 2006], to ENSO [Saravanan and Chang, 2000], and to the extratropical north Atlantic climate variability [Rodríguez-Fonseca *et al.*, 2006]. Interestingly, Figure 2

<sup>1</sup>Auxiliary materials are available in the HTML. doi:10.1029/2007JC004495.

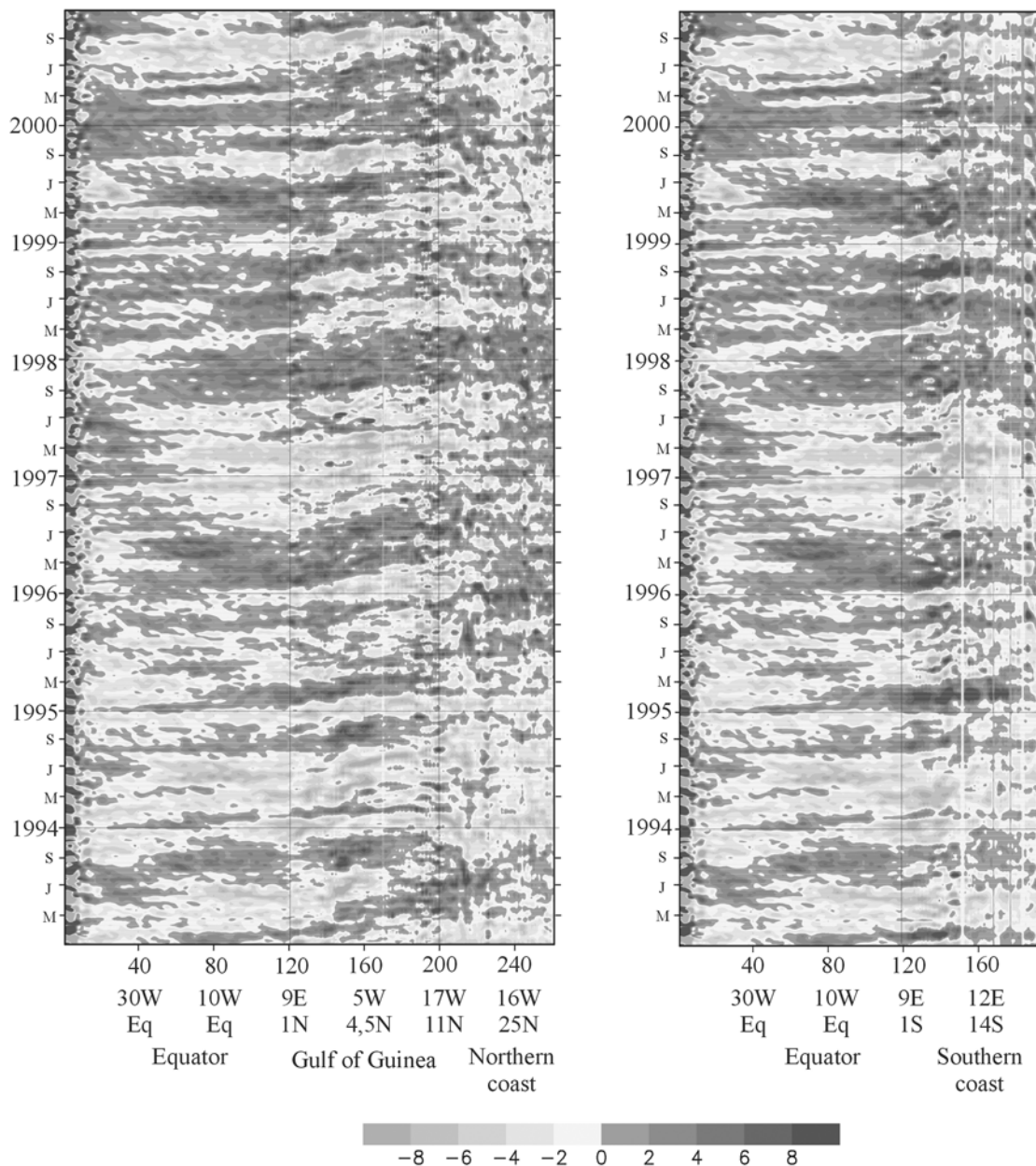


**Figure 2.** Hovmuller diagrams for the observed SSH interannual anomalies (cm), following the track of the Figure 1b, for the equator and (left) the northern African coast and (right) the southern African coast for the 1993–2000 period.

suggests a quasi-permanent intraseasonal modulation of the interannual signals. The aim of the rest of this paper is to characterize the intraseasonal SSH component.

#### 4. Selection of the Intraseasonal Frequency Band

[15] Figure 3a presents the energy spectra of the observed SSH along the wave tracks computed up to a period of 500 days. The annual and semiannual cycles appear to be the most energetic and are present along the equator and the coast; they are followed by a 120-day signal (Figure 3a, top). For periods smaller than 100 days, energy is less concentrated in a specific periodicity (Figure 3a, bottom). However, there are some relative maximums at the 100–

95 day and 60–50 day periods. Below  $\sim 30$  days, there is no energy, as expected when reaching close to the T/P time resolution. Periodicity peaks at intraseasonal scales in the Atlantic have been studied in detail by *Katz* [1997], who found enhanced variance at about 25 and 50 days, and by *Han et al.* [2008], who have found dominant spectral peaks within the intraseasonal windows at 10–40 and 40–60 days. In the Pacific, *Kessler et al.* [1995] or *Cravatte et al.* [2003] has also showed a peak at 120 days, but the next smaller period is 75 days with neither 60 day nor 95 day peaks. The SSH spectrum appears in the Atlantic with no clear single peak but rather with a wide range of active periods. As *Roundy and Kiladis* [2006] proposed for the Pacific equa-

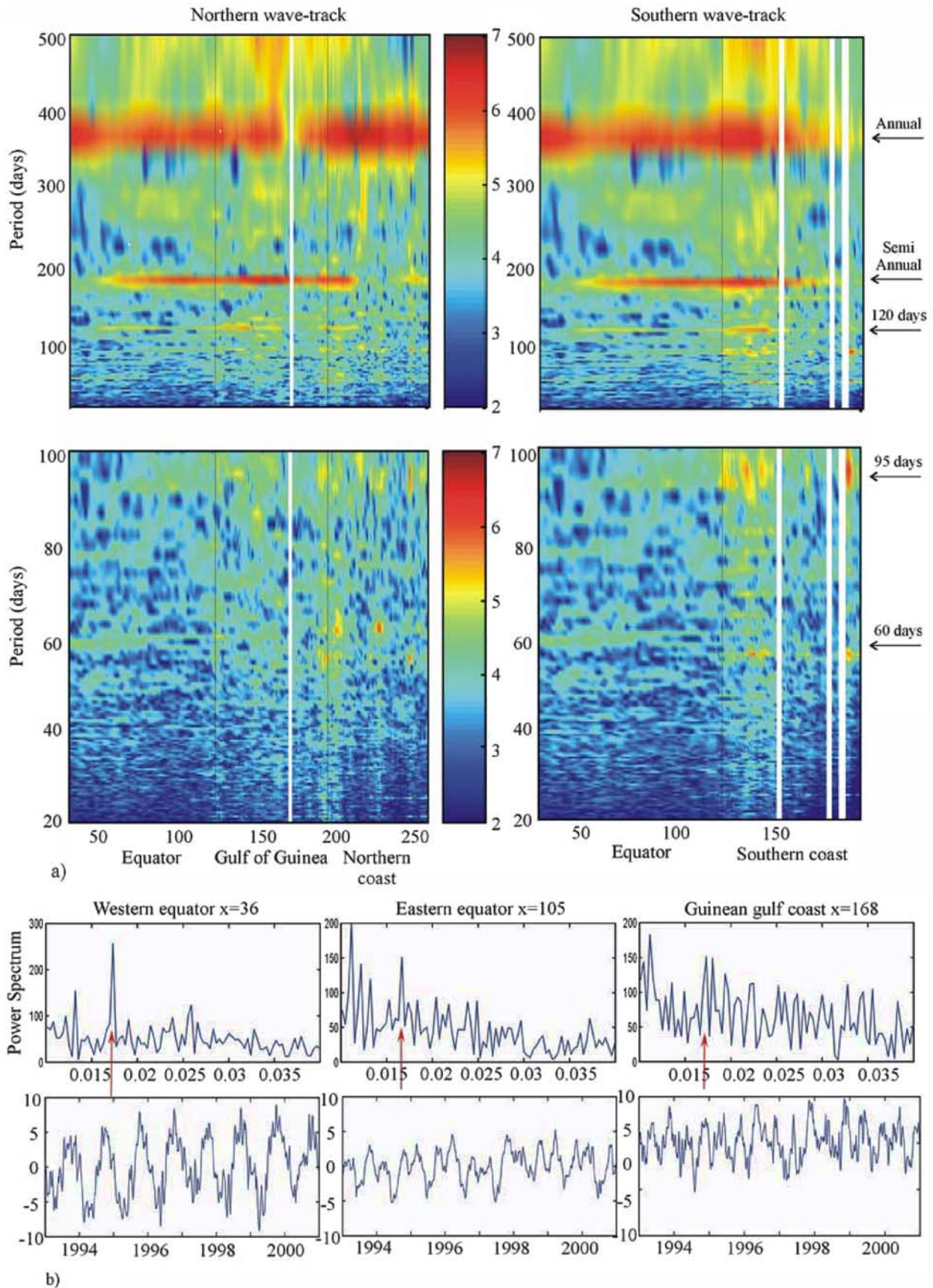
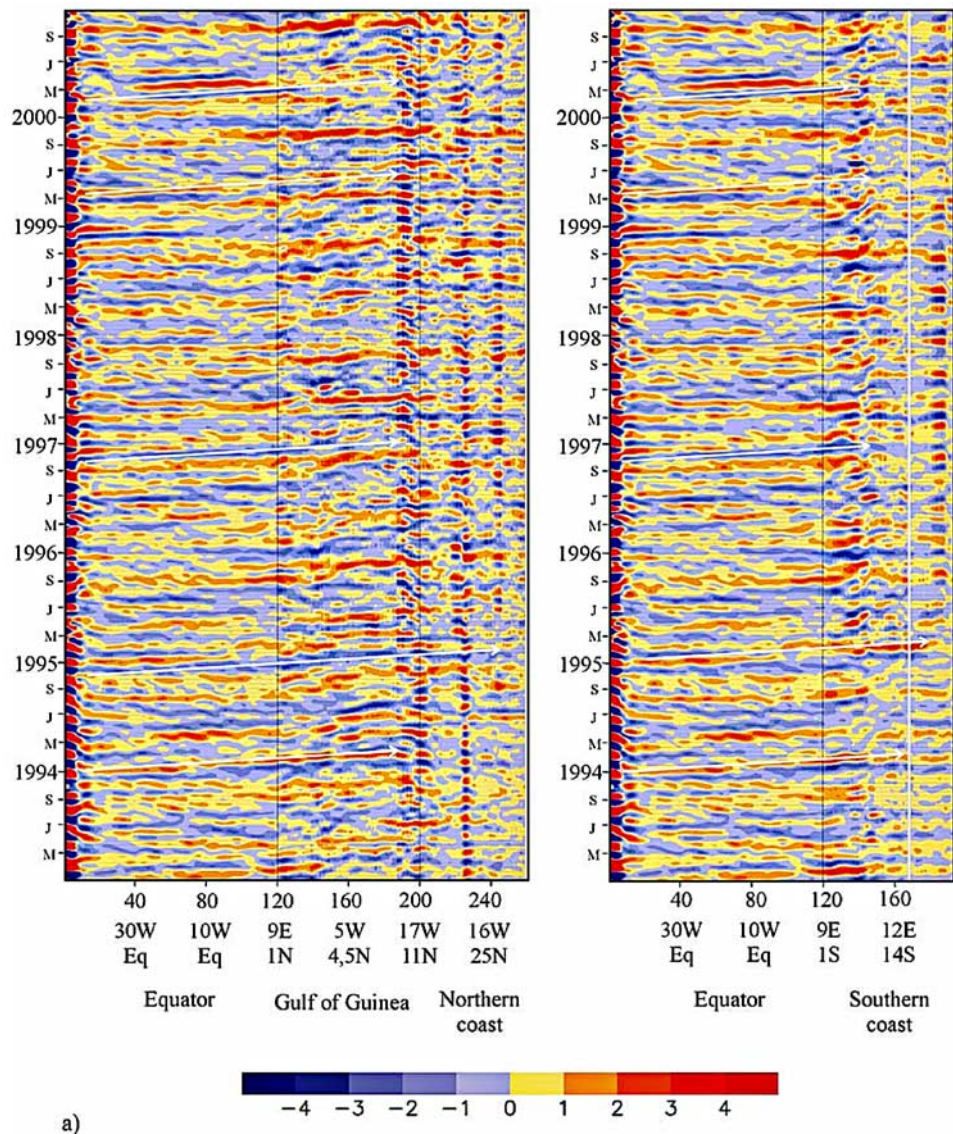


Figure 3



**Figure 4.** (a) Hovmuller diagrams of the observed intraseasonal SSH (in cm), following the wave track of Figure 2, for the equator and (left) the northern African coast and (right) the southern African coast for the 1993–2000 period. The filtered SSH signals are the result of applying a 21–91 day band-pass filter. The white arrows correspond to 1.8 m/s propagation phase speed. (b) Variance of the intraseasonal SSH anomalies for the observations (solid line) and the model (dotted line) for the north track (black lines) and the south track (gray lines). (c) Correlation between the observed and modeled intraseasonal SSH anomalies for the north wave track (black solid line) and south wave track (gray dashed line).

torial Kelvin waves, this spreading of the wave frequencies may occur in part because phase accelerations and amplitude variations are forcing the waves to become nonsinusoidal in time.

[16] Figure 3b shows an example of three points along the northern wave track ( $x = 36, 105,$  and  $168$ , which correspond to western equator, eastern equator, and GG,

respectively). Although, depending on the location, the SSH signals differ (Figure 3b, bottom), the power spectrums from 100 to 25 days show a relative peak in between 67 and 50 days (Figure 3b, top).

[17] Finally, we chose to retain the 25–95 day periodicity. The filter has been performed by subtracting two low-pass filters, which have been constructed by smoothing the

**Figure 3.** (a) Variance-preserving spectra of observed SSH data (in  $\text{cm}^2$ ). Periodicity versus track points for the (left) north and (right) south Kelvin wave track for (top) the 20–500 day periodicity range and (bottom) 0–100 day periodicity range. (b) Power spectrum ranging from (top) 20 to 100 days for three points along the north wave track corresponding to (left) the western equator, (middle) eastern equator, and (right) Gulf of Guinea and (bottom) the associated time series. The frequency around 50–66 days is indicated by an arrow.

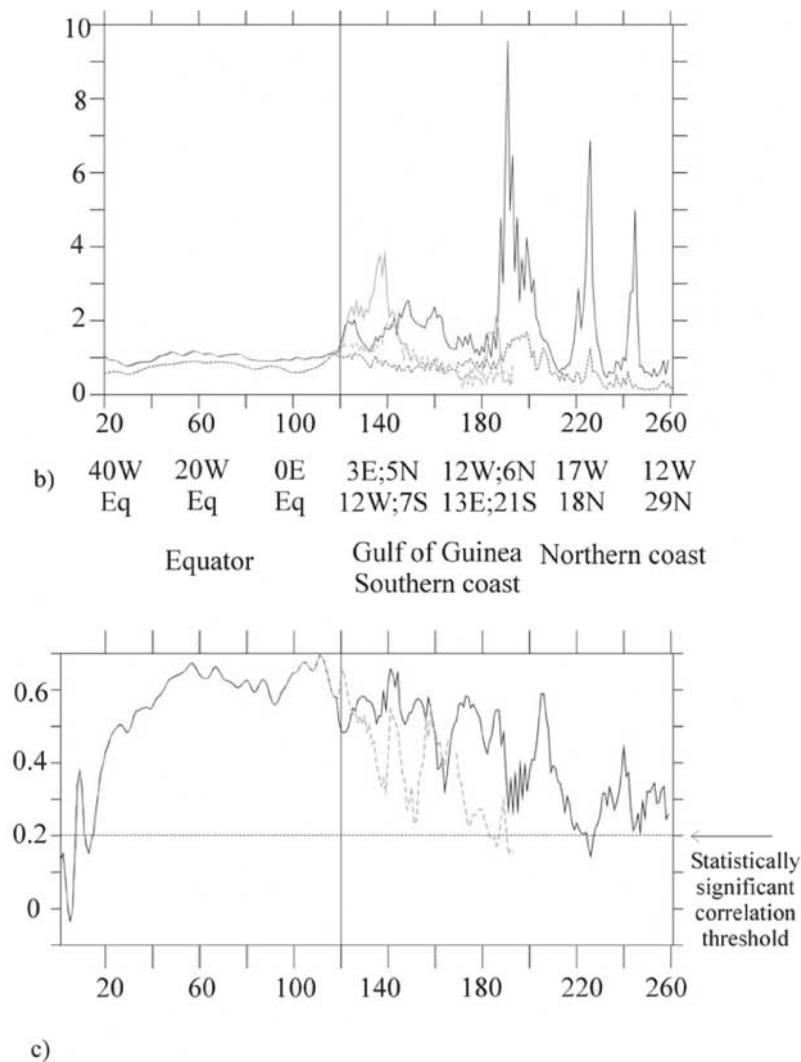


**Figure 4.** (continued)

signal with a Hanning weighting function of 21 day and 91 day time windows, respectively (25–95 days for the modeled data). The smoothing replaces each value on the grid to which they are applied with a weighted average of the surrounding data values along the time axis. The subtraction of the two low-pass filters results in a 25–95 day band-pass filter, whose frequency response function (see Figures S3 and S4 in the auxiliary material) preserves about 60% of the signal amplitude within the 70–35 day band, with a maximum (80%) at 50 days and a 10% preserving reached at about 200 and 20 day periods. Note that the filter preserves the frequencies, and it neither creates artificial spectral peaks nor phase shifts associated with negative lobes.

## 5. Description of the Intraseasonal Kelvin Wave Propagations

[18] Figure 4a shows the result of filtering the T/P SSH data in the entire period along the north (Figure 4a, left) and south (Figure 4a, right) wave tracks. The almost permanent eastward/poleward propagating signals are shown for the

year and for all the years. A first, gross visual estimation of the slopes for continuous signals suggests a regular propagation phase speed of  $\sim 1.8$  m/s. Figure 4a shows downwelling and upwelling Kelvin wave propagation with a  $\sim 2$  month period. It is important to notice that although the filter is preserving the 50 day period, the 2 month period signal is not just a filter product since Figure 3 supports the importance of the 2 month period and similar SSH signals are found when filtering the SSH within different windows (i.e., 25–150 day band, not shown).

[19] The absolute mean value of the SSH signal amplitude is 1–2 cm at the equator, and the signal is amplified to 2–4 cm at the beginning of the coast, at the coast of the GG (from north track points 120 to 180), and at the southern African coast (from south track points 120 to 150). This intraseasonal SSH signal represents  $\sim 50\%$  of the seasonal cycle amplitude (compare with Figure 1a). The SSH variance (Figure 4b) is 1 cm at the equator and increases to 2 cm at the African coast, with higher variance at some coastal track points.

[20] Although there are horizontal SSH bands (i.e., October–November 1993; October–November 1997 in

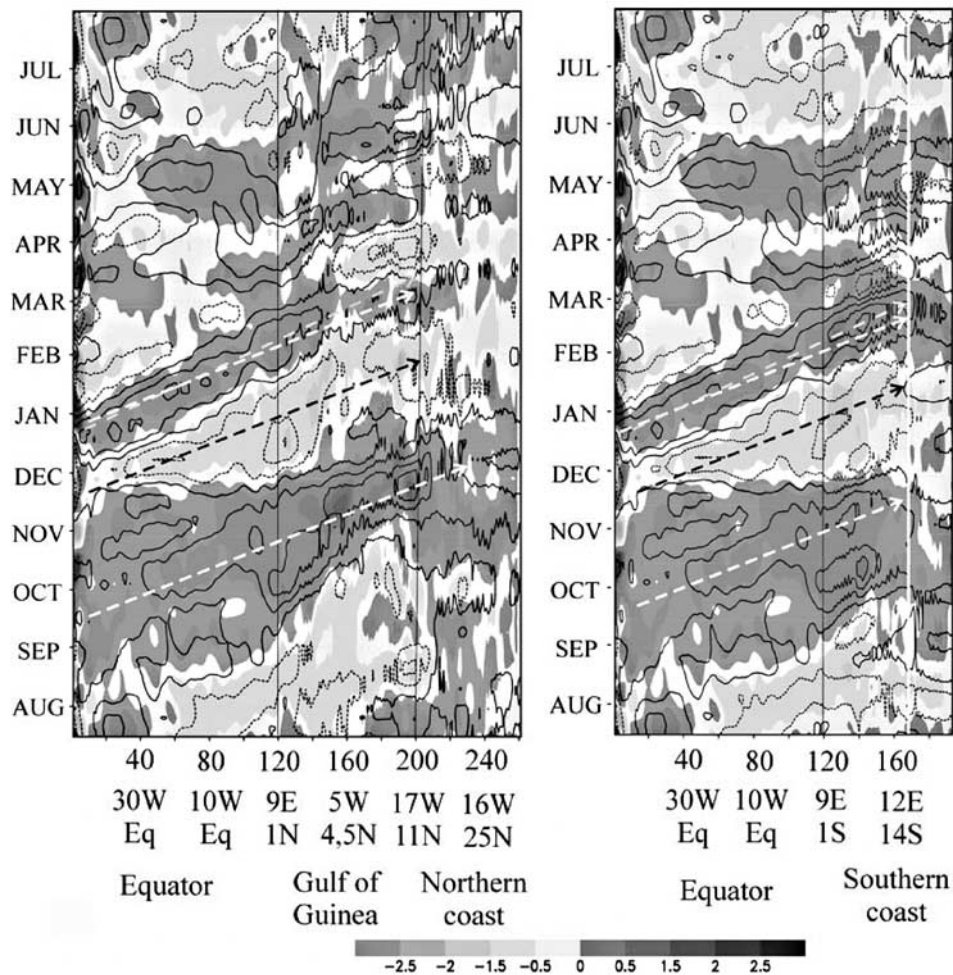


**Figure 5a.** Climatology of the intraseasonal SSH anomalies (in cm) for the observations (shaded areas) and the model (contour lines, contour interval (CI) is 0.5, the zero line has been removed) for (left) the north wave track and (right) the south wave track. The arrows correspond to 1.8 (white and black lines) and 1.6 m/s (gray line) propagation phase speeds.

Figure 4a) corresponding to whole basin equatorial events, most of the SSH signals are associated with an eastward propagation. After the equatorial Kelvin wave splits at the African coast, poleward propagation can be noticed as far as  $12^\circ$  (north track point 200 and south track point 160). Beyond these points, no propagation can be detected. Some exceptions, as for the southern track that shows clearer propagation at higher latitudes for some events (see November–December 1993 events in Figure 4a), could be due to some “in-phase” SSH variations forced locally by wind burst. This latitudinal propagation threshold is explained by the limitation of the data resolution ( $\sim 0.5^\circ$ ) versus the radius of deformation. Poleward of  $15^\circ$  latitude, the distance comprised in  $0.5^\circ$  longitude exceeds the radius of deformation computed for 2 m/s baroclinic phase speed (see Figure S1 in the auxiliary material), which makes the wave barely detectable.

[21] Strikingly, the Hovmuller diagrams repeatedly display equatorial and coastal downwelling Kelvin waves in September, December, and March, whereas equatorial and coastal upwelling Kelvin waves appear frequently in

November, January, and July. The September–November and December–January pairs are representative for most years. However, an interannual modulation of the intraseasonal variability is also clear (for example comparing autumn–winter 1994 and 1999 years in Figure 4a).

[22] The Hovmuller diagram for the modeled SSH (not shown) exhibits even clearer anomaly propagation at those frequencies than the observed SSH. In order to test the ability of the ORCA05 configuration to simulate the intraseasonal SSH, we have correlated the model and the T/P data at intraseasonal scales (Figure 4c). Along the equator the correlation is statistically significant, except for the western equatorial Atlantic, because of the noisy SSH signal in this area, as it has been discussed before (likely due to the low time resolution of the river runoff data in the model, T/P error near the Amazon mouth, or incorrect NBC rings in the model). Along the coast, the correlation is good for most of the points, decreasing poleward for the north and south wave tracks.

[23] The differences of the variances for the model and for the observations can be seen in Figure 4b, in that the

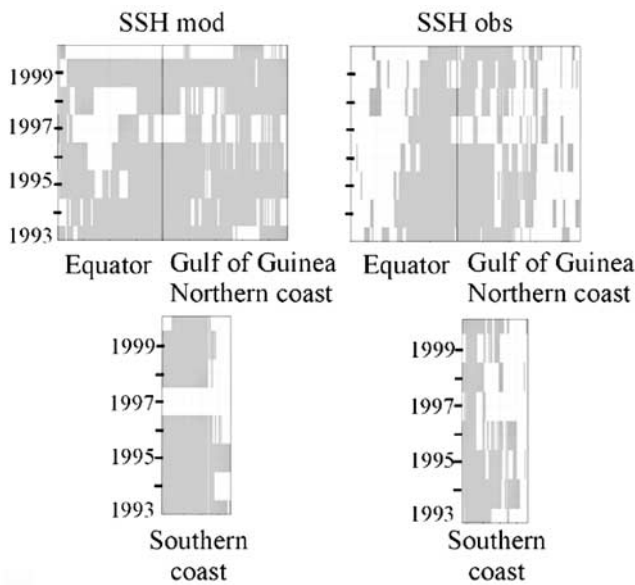


**Figure 5b.** Statistically significant areas are shaded from a significance Student's  $t$  test, at 99% confidence level, for the correlation between the sampled average of SSH (intraseasonal climatology from Figure 4a) and the temporal series for each year and for each point along (top) the north and (bottom) the south wave tracks for (left) the model and (right) the observations.

amplitude of the observations is larger than the model one. In particular, the variance differs very much for the point 190 of the north wave track, a point that is probably very affected by the tide of the 2 month period [Arnault and Le Provost, 1997]. The differences at equatorial track points 0–20 and south track point 140 are related to the Amazon (not shown because it has a very large value) and the Congo River runoff, respectively. The main differences also appear at north track points 220–240 and south track point 185, which correspond to the permanent coastal upwelling regions, likely not very well represented by the altimetry and/or due to the model resolution. Note that the correlation between the modeled and observed nonfiltered SSH data is statistically significant for all the points (not shown), although lower correlation occurs at the GG for the north wave track and at 15°S for the south wave track ( $r = 0.5$ ). Although a thorough intercomparison study between the model and the T/P data is not within the scope of our work, the statistical basic test suggests that the model configuration is suitable for the study of the SSH intraseasonal variability at the equator and the tropical African coast. Hereinafter, the model and the observations will be used in this paper to understand the SSH variability, and its dynamics will be used in paper 2.

[24] Last, it is worth noting that the Hovmuller diagram (same as Figure 4a) for the modeled  $z_{18}$  variable (not shown) displays similar characteristics in terms of propagation, suggesting that the observed SSH is a very good proxy for the study of propagations in the real thermocline. This is in agreement with studies of the relationship between sea level and stratification in the tropics, which have suggested

that a 1–2 cm rise in the sea level reflects a 2–4 m deepening of the thermocline [Carton *et al.*, 1996].

### 5.1. Intraseasonal Climatology: Main Recurring Propagation

[25] To clarify the main propagation properties described before, and particularly to bring to light the most regular intraseasonal signals, the 5 day climatological average of the band-pass-filtered SSH for the period 1993–2000 has been computed for the observations and the simulation. This intraseasonal climatology (Figure 5a) displays some events clearly related to wave propagations along parts of the tracks. The equator shows more positive propagation during the downwelling season (September to February, Figure 1a) and more negative and quite less propagating signals during the climatological upwelling season of the western basin (March to August). The most pronounced features in Figure 5a appear in the boreal autumn–winter season, in particular September and December downwelling propagations. They are associated with November and January upwelling propagations, seem to reach quite far poleward in both hemispheres, and are comparable in the model and the observations. The phase speed of these events ranges from 1.6 (gray arrow) to 1.8 m/s (white and black arrows), the latter corresponds to the one estimated from Figure 4a. The SSH slope suggests that the phase speed slows down slightly from the equator to the African coast.

[26] Despite weaker amplitude compared to the nonaveraged signals (Figure 4a), the amplitude of this climatology still represents more than 20% of the seasonal cycle amplitude (from Figure 1a). In order to represent the significance of this intraseasonal climatology for all the years considered here in observations and model, we have performed a significance parametric test under, on the one hand, the null hypothesis of “equal means” and, on the other hand, the null hypothesis of “independent fields.” Each year has been compared to the sampled mean constructed without that particular year under 95% and 99% confidence levels. The mean is statistically significant, at 95% and 99% confidence level, for all the years for observations and model and for north and south wave tracks (not shown). The correlation is statistically significant at 99% confidence level from a Student's  $t$  test for most of the years along the track (Figure 5b). The observed SSH intraseasonal climatology is significant over the central eastern equatorial Atlantic for all the years, but it is not significant at the western equatorial Atlantic and subtropical regions (Figure 5b, right). Regarding the model, the intraseasonal climatology is not significant for some particular years (1997, 1998, and 2000) over the central equatorial Atlantic (Figure 5b, left). The year 1997 does not seem to be significant mostly along both north and south wave tracks and for observations and model. The most significant regions for both observations and model are the central eastern equatorial Atlantic, the GG, and the southern coast from the equator down to 12°S.

[27] In order to assess the thermocline vertical displacements associated with the SSH anomalies, the intraseasonal climatology of the 18°C isotherm depth is presented in Figure 5c (the intraseasonal climatology of the modeled SSH is also superimposed). Whereas the consistency between the SSH and the  $z_{18}$  is high, the latter is often

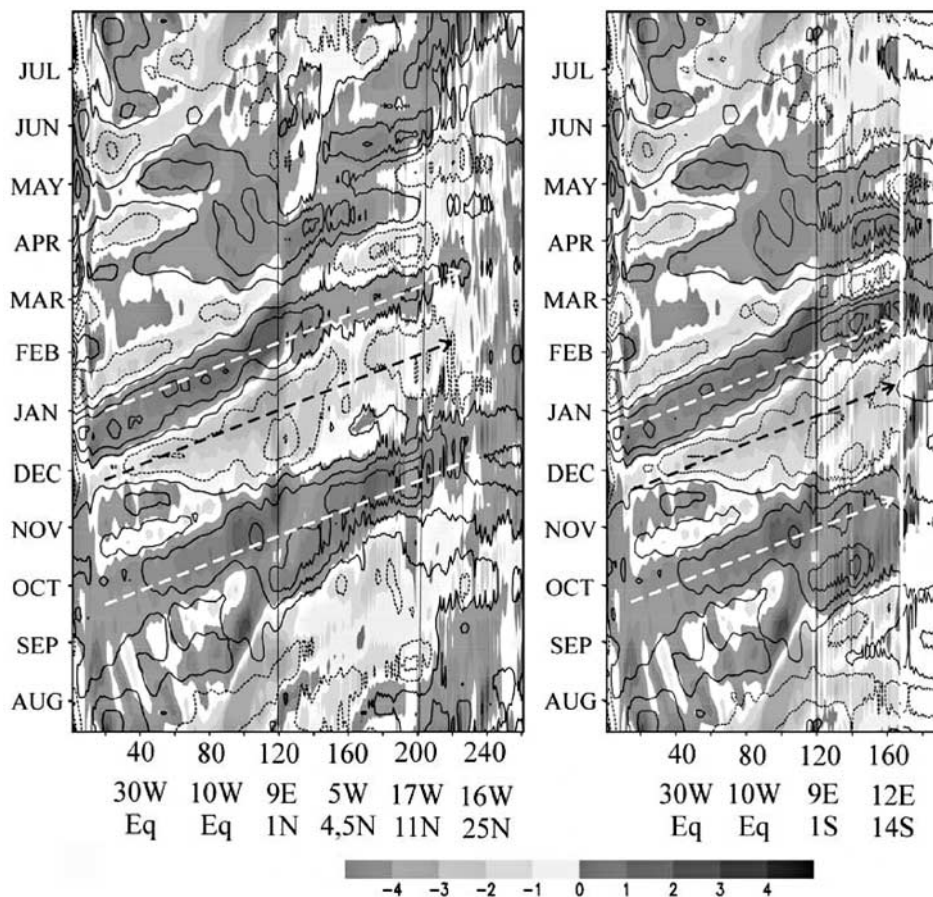


**Figure 5c.** Climatology of the intraseasonal  $18^{\circ}\text{C}$  isotherm depth anomalies (shaded areas, in m) and modeled intraseasonal SSH anomalies (contour lines, CI is 0.5 cm, the zero line has been removed) for (left) the north wave track and (right) the south wave track. The arrows correspond to 1.8 m/s propagation phase speed.

more continuous from the equator to the coast and farther north and south than the former (see the December downwelling wave that reaches the most northern point at approximately constant speed). Note that the SSH and z18 are more in agreement over the equatorial band than poleward of  $10^{\circ}$  latitude where the SSH-z18 relation is more complex, likely because of larger compensation effects by additional thermodynamical processes such as surface heat fluxes [Mayer *et al.*, 2001].

[28] From z18 intraseasonal climatology (Figure 5c), the August–September downwelling Kelvin event can be seen as a particular wave starting at the African coast rather than propagation from the western equator. At this event there is a different behavior of the SSH and z18; the z18 splits between the equator and the GG, and it is interpreted as a split of modes, which is coherent with the results of Illig *et al.* [2004]. Once trapped at the coast, SSH and z18 September and December downwelling signals appear to be amplified at the coast of the GG (north track points 140–200) and at the southern coast (south track points 120–160). This amplification was also noticeable over the whole 1993–2000 period for the T/P SSH and its variance (Figures 4a (left) and 4b). The propagation pattern disappears at north track point 215 and south track point 170, and

beyond these points (near subtropics) the signal seems to be stationary (Figures 4a, 5a, and 5c).

[29] To isolate and to quantify the spatial-temporal structure of the robust September to February Kelvin waves, we present in section 5.2 an extended principal component analysis.

## 5.2. A Mode for Boreal Autumn–Winter Intraseasonal Kelvin Waves

[30] A canonical mode of the boreal autumn–winter Kelvin waves can be established thanks to a discriminant analysis technique known as extended empirical orthogonal function (EEOF), which constitutes an extension of the traditional EOF technique. It deals not only with spatial but also with temporal correlations observed in weather/climate data [Weare and Nasstrom, 1982], and it is suitable to the study of oscillatory phenomena [Fraedrich *et al.*, 1997]. We consider positive and negative lagged time series for each track point, and we apply an EOF analysis of this pool of time series. The EEOF analysis recognizes that the temporal evolution of the spatial patterns is an integral part of a system’s development. Consider a track time section (Hovmuller), which can be described by a vector of  $\mathbf{K}$  components ordered according to the track and evolving

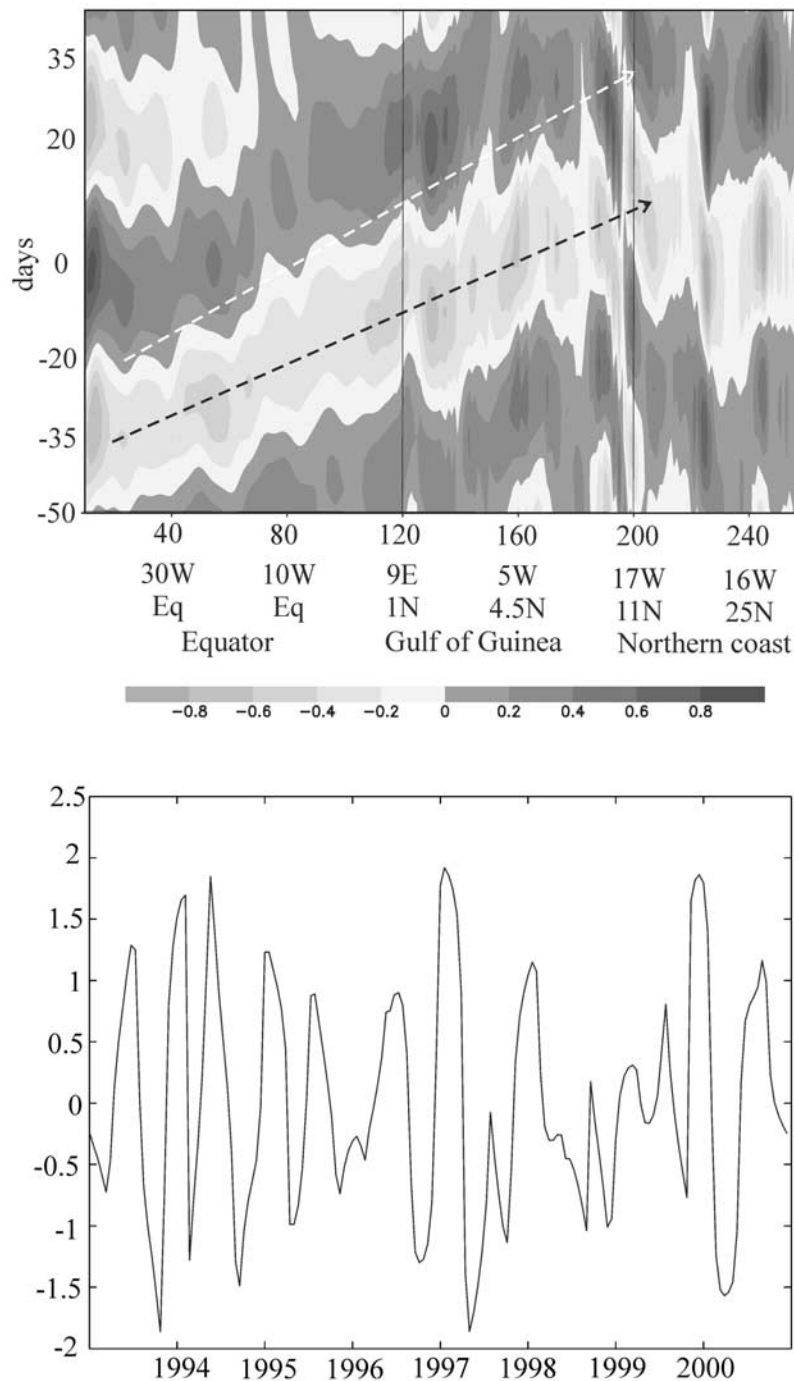


**Figure 6.** (top) Leading extended empirical orthogonal function mode of the observed intraseasonal SSH along the north wave track (in cm) and (bottom) the associated extended principal component for the period 1993–2001 in boreal autumn–winter (September to February). The EEOF has been performed after interpolating the T/P SSH to 5 day temporal outputs and obtaining 21 lags. The white (black) arrow corresponds to 2 m/s (2.5 m/s) propagation phase speed.

with time. Sliding a time window of length  $W$  over this vector time series leads to a new vector; this vector represents the states of the system in a  $K \times W$  dimensional phase space spanned by time delay coordinates.

[31] As shown previously, autumn–winter is a particularly active season for the Kelvin waves; therefore, the EEOF analysis is performed for the boreal autumn–winter

season (from September to February) for all the years from 1993 to 2000. The EEOF analyses are performed on time wave track series of observed filtered SSH, applying a window of 5 days to the data to obtain 21 lags, and thus calculating the EOFs of the time development of the Kelvin wave track structure. From the analysis, a resultant total extended principal component (EPC) index is computed,

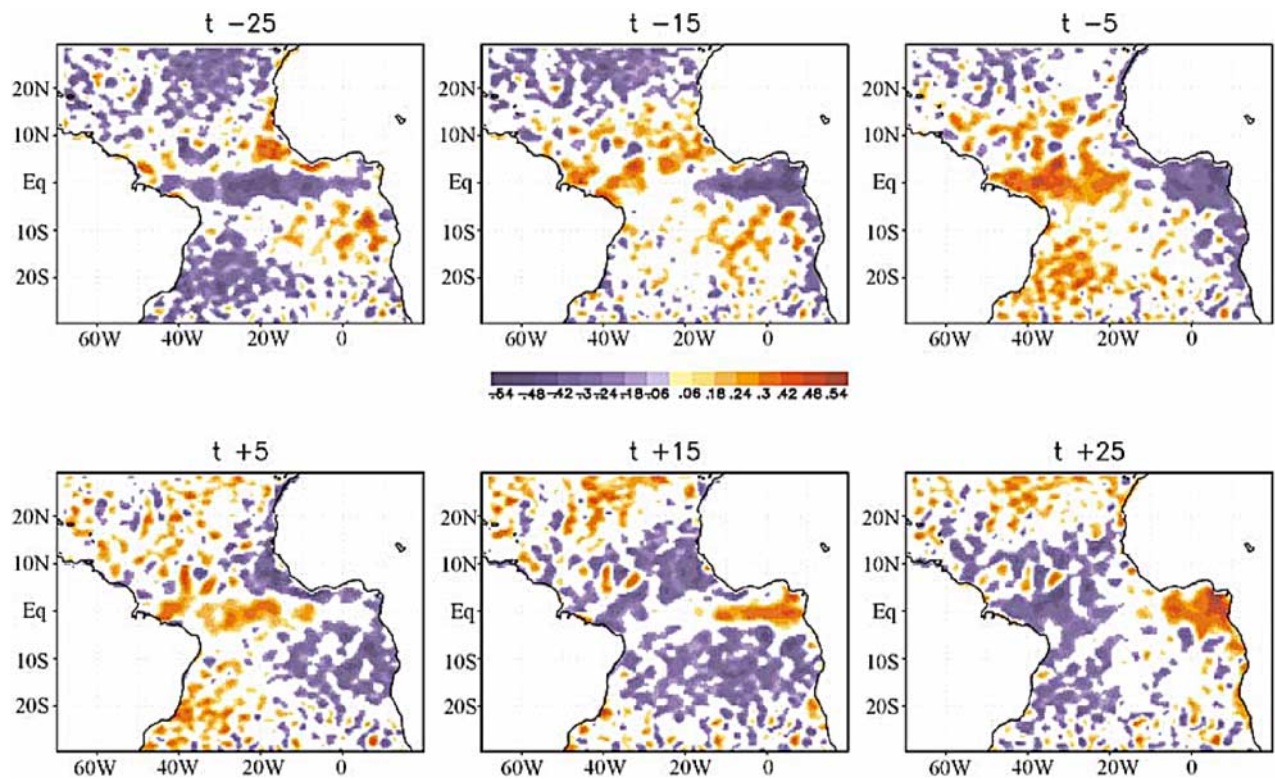


**Figure 7.** Regression of the observed intraseasonal SSH anomalies over the whole tropical Atlantic on the leading EEOF mode from Figure 6 at different lags (in cm). Only statistically significant areas at 95% confidence limit are plotted.

which is projected onto the original field to represent the EEOF spatial pattern. For simplicity, only the north wave track is analyzed since both north and south wave tracks share the equatorial Atlantic and the leading mode of the south wave track (not shown) is highly correlated with the leading mode of the north wave track.

[32] The leading EEOF variability mode of boreal autumn–winter filtered T/P SSH, which explains 10% of the variance of the filtered signal, is shown in Figure 6. It shows the upwelling–downwelling Kelvin waves along the equator and the coast of the GG (Figure 6, top). The SSH anomalies propagate from the western equator to  $\sim 15^\circ\text{N}$  (track point 220) at a rather stable speed ranging from 2 to 2.5 m/s, a higher phase speed than the one estimated from the previous Hovmuller plots (Figures 4 and 5). Farther north, in the subtropical coastal region, other processes seem to explain the SSH variability, as discussed in section 5.1. The leading EPC (Figure 6, bottom) shows one cycle per autumn–winter of positive and negative SSH over the wave track. The remarkable interannual modulation of the EPC index is in agreement with those noticed in Figure 4a. Although special years of variability are found for the 1996–1998 period, the main periodicity of the wave from the EEOF analysis is around 50 days. The second mode (not shown) corresponds to Kelvin wave propagation along the western central equatorial Atlantic (in quadrature-like with the leading mode) but without continuity along the coastal wave track.

[33] In order to visualize the spatial structure of the leading EEOF mode, the observed SSH over the whole TA basin has been regressed onto the EPC, and it is shown in Figure 7. The projection has been done for different lags (lagging the SSH field from  $-25$  days to  $+25$  days) to show the time evolution over the whole TA as the wave is propagating. The projection shows very clear spatial structure for the beginning of the downwelling (upwelling) equatorial Kelvin wave at the western equator at lag  $-15$  (lag  $+15$ ). The Kelvin wave propagates trapped at the equator at lag  $+5$  (lag  $-25$ ), reaching the African coast at lag  $+25$  (lag  $-5$ ). At the Guinean Dome and  $5^\circ\text{S}$ , a Rossby wave-like radiation is visible propagating westward at lag  $-15$  (lag  $+15$ ). Finally, the coastally trapped Kelvin wave propagates as far as  $\sim 15^\circ$  latitude at lag  $-25$  (lag  $+5$ ).

[34] The EEOF analysis has discriminated a very robust propagating pattern associated with equatorial and coastally trapped Kelvin waves. We have shown the importance of the intraseasonal propagating signals, particularly in boreal autumn–winter, with different methodologies. The EEOF information will be used in paper 2 to study the associated air–sea interactions.

## 6. Finer Estimates of Propagation Phase Speed and Teleconnections

[35] Once the intraseasonal climatology and the leading boreal autumn–winter mode are underlined, it is worth coming back to the intraseasonal time series through a lead

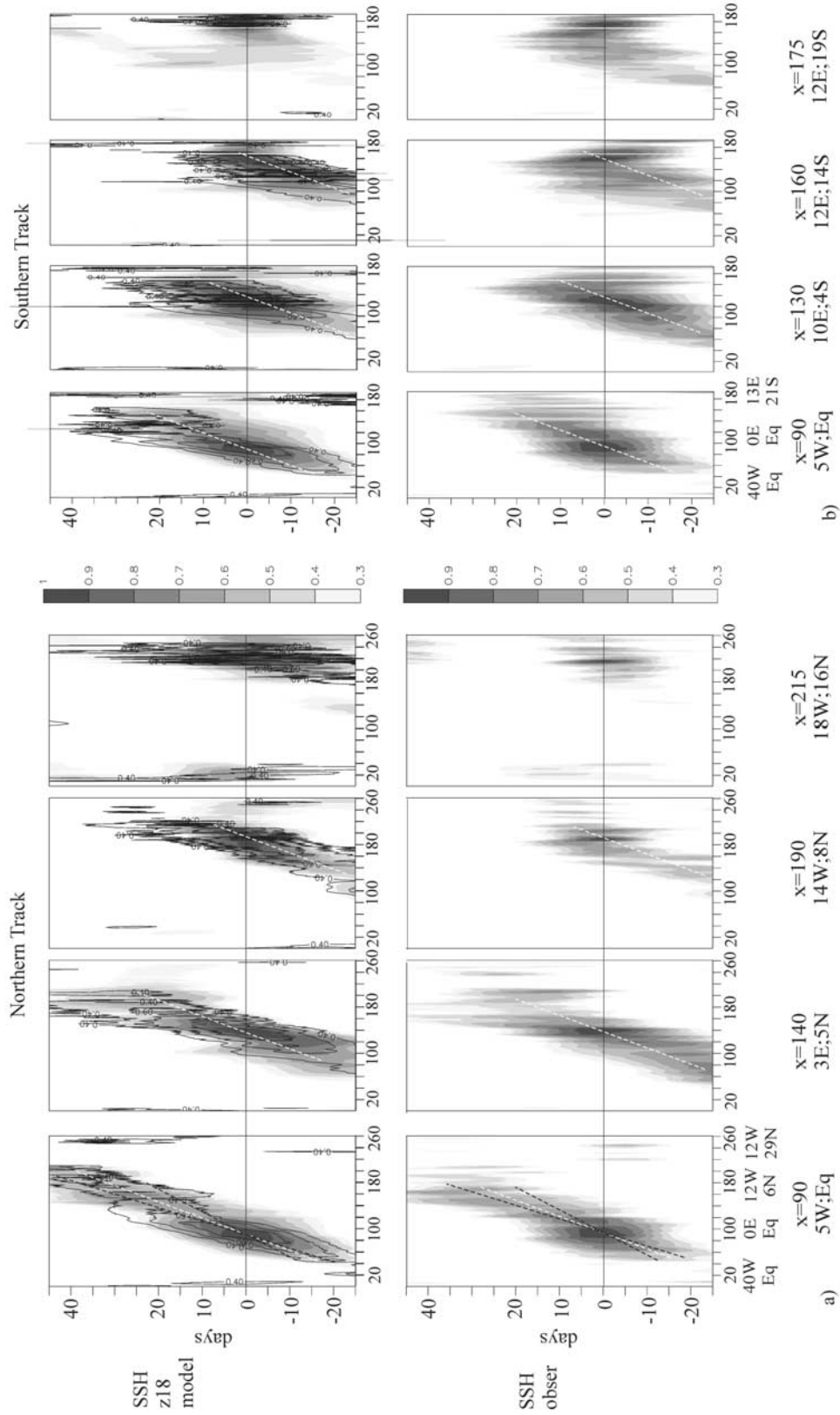


**Figure 8.** (a) One-point observed SSH (shaded) and modeled z18 (contour lines) intraseasonal climatology lag correlation map for several track points for the north and for (top) the model and (bottom) the observations. Correlation significant at the 99% confidence limit is plotted. The black, white, and black lines correspond to 2.5, 1.8, and 1.5 m/s propagation phase speeds, respectively. (b) Same as Figure 8a but for the south African coast wave track.

**Table 1.** Phase Speed Calculated by Linear Best Fitting and Radon Transform of the Observed and Modeled SSH of the North and South Wave Tracks<sup>a</sup>

Hovmuller SSH Field	Phase Speed (m/s)	
	From Linear Fitting	From RT
Modeled north	1.6	1.60
Observed north	1.5	1.86
Modeled south	1.8	1.86
Observed south	1.9	2.10

<sup>a</sup>Linear best fit has been computed and averaged from Figure 8. The RT has been computed for each Hovmuller diagram for the observed (from Figure 4) and modeled SSH, with smoothing Hanning window, avoiding the signals around the frame. The RT of the images has been performed for angles between  $-90^\circ$  and  $90^\circ$  every  $0.05^\circ$ .

lag correlation analysis. It allows for both a finer quantification of the phase speed and the teleconnections sustained by the waves.

### 6.1. Propagation Phase Speed

[36] The speed of oceanic wave propagation is important in determining the oceanic response time to disturbances from the equilibrium state. A thorough estimate also offers a sound way to evidence the wave nature of the apparent propagations in the band-pass-filtered data. The equatorial Kelvin wave has a phase speed defined by the linear theory as

$$c_n = (gh_n)^{1/2},$$

where  $h_n$  is the equivalent depth for each  $n$  mode. The Atlantic equatorial Kelvin wave propagations have been shown in observational data and linear theory to have a phase speed range of 2.4–2.9 m/s for the first baroclinic mode, 1.2–1.5 m/s for the second mode, and 0.8–1 m/s for the third mode [Du Penhoat and Treguier, 1985; Philander, 1990; Katz, 1997; França *et al.*, 2003; Illig *et al.*, 2004; Guivarc’h *et al.*, 2008].

[37] Figure 8 shows the one-point lag correlation for the intraseasonal climatology shown in Figure 5, at 99% confidence level, for the modeled (Figure 8, top) and the observed (Figure 8, bottom) SSH and z18 variables. We have chosen four different points along the north (Figure 8a) and south (Figure 8b) wave track corresponding to different regions: eastern equator, GG, southern African coast, and subtropical regions. The lag correlation for z18 is also shown in contours, giving a similar phase speed than the one from the SSH. At the subtropics (i.e., the north track points 220–260 and the south track points 160–190), the slope tends toward zero as the SSH signal shows nearly horizontal structure poleward of  $\sim 12^\circ$  latitude for both model and observations (as shown in Figures 4a, 5a, and 6).

[38] The phase speed can be easily computed by linear regression of the maximum correlations at each point and lag in Figure 8. The different linear fittings corresponding to 2.5, 1.8, and 1.5 m/s are included in Figure 8. The visual comparison with the arrows indicates that the observed climatological Kelvin wave phase speed ranges from 1.5 to 2 m/s. Because of the large dispersion of the data in the lag correlation plots, we have also computed the phase speed with radon transform (RT) methodology, which is a more

accurate technique. The RT is a very useful image processing technique for the satellite images, and it has been used before to characterize the phase speed of the oceanic Rossby waves [Chelton and Schlax, 1996; Polito and Cornillon, 1997; Hill *et al.*, 2000; Challenor *et al.*, 2001]. To compute the RT of the track time plot (Hovmuller) for different values of direction is equivalent to computing the energy in the spectrum along lines of constant speed, and it is the most straightforward method for finding the value of the speed for which that energy is maximum [Challenor *et al.*, 2001]. The corresponding angle of the maximum RT standard deviation is defined as the angle of the propagation. The methodology has been applied following Hill *et al.*'s [2000] work for the observed and modeled SSH Hovmuller and for the north and the south wave track in the entire 1993–2000 period (Table 1). The phase speed calculated by RT, on average, does not significantly change the phase speed calculated by linear regression of the maximum lag correlation. The propagation phase speed ranges from 1.5 to 2.1 m/s, which is also found by other authors [Katz, 1997; França *et al.*, 2003], and it could correspond to a mix between the first and the second theoretical Kelvin baroclinic modes or a modulation of the first baroclinic Kelvin wave mode speed by the first baroclinic Rossby wave mode. In addition, topography effects, stratification changes, and the blend of modes can intricately be disturbing the measurements. It is important to notice that performing the RT for each point results in important variations along the tracks (not shown), especially from the equator to the coast, which can also be observed from Figures 4a, 5a, and 8. The differences between the observed and the theoretical phase speed, as well as the speed variations along the wave track, will need further investigation.

[39] Nevertheless, the velocities found for both north and south wave tracks for the modeled and the observed SSH and with different methods show a satisfactory agreement of the model with the satellite estimates (Table 1). This means that even with a low resolution, the model is suitable to study oceanic Kelvin wave propagations, at least equatorward of about  $12^\circ$  latitude. Overall, the amplitude (Figures 4b and 5a) and the phase speed (Figure 8) are both important wave factors and are well reproduced by the OGCM simulation. This result will be important to the diagnosis of the forcing mechanisms in paper 2.

[40] From the calculated phase speed, we can conclude that the Kelvin wave propagation seen in Figures 4, 5, and 6 is expressing mainly the first two baroclinic Kelvin wave modes along the equator and the African coast.

### 6.2. How Far Kelvin Wave Travels: Evidence for Teleconnections

[41] Figure 8 can also be used to quantify how SSH intraseasonal variability along the coast and as far as about  $12^\circ$  (around north track point 200 and south track point 150) is remotely controlled by the wave propagating signal.

[42] In Figure 8, we consider that the teleconnection breaks down where the apparent slope changes drastically, in particular, where it becomes more horizontal. Although the lag correlation decreases with distance away from the point and the propagation direction is difficult to discern because of the large physical processes implied, an equatorial connection driving SSH anomalies along the coastal

track can still be seen. Hence, starting with the northern coastline, the correlation centered at  $5^{\circ}\text{W}-0^{\circ}\text{N}$  (track point 90) shows continuity from the equator to the coast, although there is a change in the slope at the coast of the GG as noted previously (Figures 4, 5, and 6) ( $\sim 120$  track point transition between the equatorial and coastal waveguide), and the slope break latitude is reached at about  $10^{\circ}\text{N}$  (track point 195) with a correlation of about 0.4. The correlation pattern suggests that this equatorial point still remotely controls 16% of the intraseasonal variance at  $\sim 10^{\circ}\text{N}$ . The correlations centered at  $3^{\circ}\text{E}$  over the GG (north track point 140) indicate, as expected, a clear control from the eastern equator, as well as a significant impact in the propagation direction up to  $\sim 16^{\circ}\text{W}$ ,  $10^{\circ}\text{N}$  (north track point 195) in the observations and farther poleward in the model. At these latitudes, the explained variance drops down to about 10–20%. In Figure 8a, centered at  $14^{\circ}\text{W}-8^{\circ}\text{N}$  (track point 190), the correlations for the observations show that the point is partly controlled by equatorial locations farther behind it, but no signal seems to propagate farther north. Beyond  $12^{\circ}\text{N}$  (Figure 8a, track point 215), the SSH is more related to neighboring points at lag zero, suggesting other types of coherent local forcing.

[43] For the south (Figure 8b), the correlation shows even more continuity between the equator and the coast than for the north, probably due to the straighter coastline. The correlation slope appears to break in the vicinity of  $12^{\circ}\text{S}$  (track point 150). Beyond this point the correlation is significant but the slope is not coherent, with a teleconnection via Kelvin wave propagations. This suggests a control by other processes. The lack of propagation beyond  $12^{\circ}\text{S}$  is seen to be clearer for z18 (Figure 8b (top), track point 175), while the observed SSH (Figure 8b (bottom), track point 175) shows more correlation with the equatorial points.

[44] In conclusion, the T/P SSH supports the importance of teleconnection through Kelvin waves along the tropical African coast from the equator up to  $12^{\circ}\text{S}$  and  $10^{\circ}\text{N}$  ( $12^{\circ}\text{N}$  in the model). These latitudinal teleconnection thresholds could be due, in part, to the limits of the data resolution relative to the Rossby radius of deformation (close to  $15^{\circ}$  latitude). They are likely associated with the location of the intense coastal Mauritanian/Senegal and Angola/Benguela upwelling systems. Roughly, it is in the vicinity of  $10^{\circ}$  latitude, depending on the season, where the isopycnal surfaces start to outcrop in these upwelling regions. Hence, the signals carried out by the waves are partly transferred into the mixed layer and correspondingly limit the ability of the waves to propagate information.

[45] In practice, because of the dissipative effects, there should be a limit to the distance to which the information is carried poleward by waves [Gill, 1982; Clarke and Shi, 1991]. The lack of correlation at higher latitudes could be because a great deal of energy is also found in smaller-scale motions; these may be eddies, wave motions due to small-scale features by bottom topography, or loss of energy by Rossby wave radiation from the African coast [Mittelstaedt, 1991]. Last, the orientation relative to the coast, the regularity, and intensity of the trade winds exhibit major changes between the deep tropics, equatorward of  $10^{\circ}\text{N}$ , and the tropical-subtropical regions. We will show in paper 2 that the SSH variability poleward of  $12^{\circ}$  latitude is essentially

controlled by local wind to the expense of teleconnection processes.

## 7. Conclusions

[46] This paper is an attempt to provide new and sound insights into TA intraseasonal Kelvin wave activity. This topic has received less consideration than the Pacific basin [Kessler *et al.*, 1995; Cravatte *et al.*, 2003; Roundy and Kiladis, 2006]. It is essential to investigate it thoroughly in light of the recent Aviso T/P data set and state of the art OGCM, considering how often remote forcing by Kelvin waves is invoked to interpret TA variability, particularly in the vicinity of the Angola/Benguela upwelling system [Florenchie *et al.*, 2003; Rouault *et al.*, 2007], as well as in the coast of the GG [Servain *et al.*, 1982; Picaut, 1983; Aman *et al.*, 2007].

[47] In order to study the SSH intraseasonal variability, we have band-pass filtered the data in the 25–95 day period, emphasizing the relative active 50 day period. This processing, frequently used along the equator, here enlightens the propagation of Kelvin wave signals poleward along the African coast. In this paper, we demonstrate the possibility of visualizing equator to coast propagations of observed and modeled SSH and thermocline intraseasonal anomalies over several years in the TA. The TOPEX/POSEIDON and  $0.5^{\circ}$  resolution OGCM simulation data sets have proved to be suitable for the identification and characterization of equatorial Kelvin waves and their continuity within the tropical band as coastally trapped Kelvin waves at intraseasonal frequencies. Such signals can clearly be followed over a distance of thousands of kilometers along the coasts, especially equatorward of  $10^{\circ}-15^{\circ}$  latitude. However, the filter reduces the variance of the total signal by about a factor of 2, down to 1 cm at the equator and 2 cm along the coast.

[48] The estimated propagation phase speeds are found to be in the range between the first and second theoretical Kelvin baroclinic modes (from 1.4 to 2.6 m/s). The results are homogenous for the observed and modeled SSH, for the northern and the southern wave tracks, and from the different methodologies (RT and linear regression). Nevertheless, a finer understanding of the phase speeds and the thermocline response would require a modal analysis along the coast.

[49] In addition, lag correlation plots allow for the quantification of the remote effects of the waves along the coast. It is possible to state that the eastern equator SSH can explain about 25% of the intraseasonal variability of the GG so-called coastal upwelling and 16% of the intraseasonal variability of the Benguela upwelling. Although the SSH variability over the Mauritanian/Senegal upwelling region is less influenced by the wave propagations, the results support the existence of a remote forcing via eastward and poleward intraseasonal Kelvin waves of the lowest latitudes of the north and southeastern tropical upwellings.

[50] The major result of our study is the demonstration that it is possible and useful to simplify the complex intraseasonal activity down to two synthetic signals: an intraseasonal climatology and an EEOF mode. From the intraseasonal climatology, a particularly striking result is that major Kelvin wave activity occurs with a high degree of

recurrence in the boreal autumn–winter season (September–December downwelling and November–January upwelling Kelvin waves). The model simulation helped to quantify the associated stratification changes, which are very well correlated and reach a few meters for a few centimeters surface signals. The most robust continuity develops in early boreal winter from the west equator eastward and poleward toward the Benguela upwelling system and the coast of the GG in late boreal winter in observed and modeled SSH (Figure 5a) as well as within the thermocline (Figure 5c). The connecting signals propagation velocity,  $\sim 1.8$  m/s, supports the existence of some remote forcing via Kelvin waves.

[51] The extended EOF mode for this boreal autumn–winter Kelvin wave propagation is the second synthetic view of this phenomenon. The mode, albeit of weak amplitude, provides an associated spatial structure that proves well the Kelvin wave nature of these teleconnections. The fact that Kelvin wave appears as a mode achieves the importance of the waves in the context of the TA SSH variability. Its principal component time series can be used to identify interannual modulations, as well as to construct associated signals through regression onto pertinent variables, such as the wind stress and SST, which will be presented in paper 2.

[52] In order to develop a detailed description of SSH propagations and coastal teleconnections in this paper, we have left aside the analysis of the complementary process controlling the SSH: the local atmospheric forcing. In paper 2, we will focus on the causes for the equatorial Kelvin wave triggering at the western equatorial Atlantic, its relationship with the atmosphere, the possible impacts on the SST, and the particular behavior in the subtropics.

[53] **Acknowledgments.** We would like to thank to the Editor Raghu Murtugudde and anonymous reviewers for their helpful comments on the manuscript. We are grateful to Christian Ethe and Gurvan Madec for kindly providing the model run outputs and Gildas Mainsant for his help in the analysis. We also thank Serge Janicot, Vincent Echevin, and Frédéric Vivier for stimulating discussions. This study has been supported by ANETUS (CNES/NASA OSTST program) and the Spanish MCYT CGL2006–04471 and REN2002–03424 programs, which has also funded Irene Polo and her research stage at LOCEAN laboratory as part as her Ph.D. thesis.

## References

- Adamec, D., and J. J. O'Brien (1978), The seasonal upwelling in the Gulf of Guinea due to remote forcing, *J. Phys. Oceanogr.*, *8*, 1050–1060, doi:10.1175/1520-0485(1978)008<1050:TSUITG>2.0.CO;2.
- Aman, A., L. Testut, P. Woodworth, T. Aarup, and D. Dixon (2007), Seasonal sea level variability in the Gulf of Guinea from altimetry and tide gauge, *Rev. Ivoir. Sci. Technol.*, *9*, 105–118.
- Arnault, S., and R. E. Cheney (1994), Tropical Atlantic sea-level variability from Geosat (1985–1989), *J. Geophys. Res.*, *99*, 18,207–18,223, doi:10.1029/94JC01301.
- Arnault, S., and C. Le Provost (1997), Regional identification in the tropical Atlantic Ocean of residual tide errors from an empirical orthogonal function analysis of TOPEX/POSEIDON altimetric data, *J. Geophys. Res.*, *102*, 21,011–21,036, doi:10.1029/97JC00983.
- Arnault, S., Y. Menard, and J. Merle (1990), Observing the tropical Atlantic Ocean in 1986–1987 from altimetry, *J. Geophys. Res.*, *95*, 17,921–17,945, doi:10.1029/JC095iC10p17921.
- Arnault, S., L. Gourdeau, and Y. Menard (1992), Comparison of the altimetric signal with in-situ measurements in the tropical Atlantic Ocean, *Deep Sea Res., Part A*, *39*(3–4), 481–499, doi:10.1016/0198-0149(92)90084-7.
- Berliand, M. E., and T. G. Strokina (1980), Global distribution of the total amount of clouds, report, 71 pp., Hydrometeorological Publ. House, St. Petersburg, Russia.
- Carton, J. A., X. H. Cao, B. S. Giese, and A. M. daSilva (1996), Decadal and interannual SST variability in the tropical Atlantic Ocean, *J. Phys. Oceanogr.*, *26*, 1165–1175, doi:10.1175/1520-0485(1996)026<1165:DAISVI>2.0.CO;2.
- Challoner, P. G., P. Cipollini, and D. Cromwell (2001), Use of the 3D radon transform to examine the properties of oceanic Rossby waves, *J. Atmos. Oceanic Technol.*, *18*(9), 1558–1566, doi:10.1175/1520-0426(2001)018<1558:UOTRIT>2.0.CO;2.
- Chelton, D. B., and M. G. Schlax (1996), Global observations of oceanic Rossby waves, *Science*, *272*, 234–238, doi:10.1126/science.272.5259.234.
- Clarke, A. J. (1979), On the generation of the seasonal coastal upwelling in the Gulf of Guinea, *J. Geophys. Res.*, *84*, 3743–3751, doi:10.1029/JC084iC07p03743.
- Clarke, A. J. (1983), The reflection of equatorial waves from oceanic boundaries, *J. Phys. Oceanogr.*, *13*, 1193–1207, doi:10.1175/1520-0485(1983)013<1193:TROEWF>2.0.CO;2.
- Clarke, A. J., and C. Shi (1991), Critical frequencies at ocean boundaries, *J. Geophys. Res.*, *96*, 10,731–10,738, doi:10.1029/91JC00933.
- Cravatte, S., J. Picaut, and G. Eldin (2003), Second and first Kelvin modes in the equatorial Pacific at intraseasonal timescales, *J. Geophys. Res.*, *108*(C8), 3266, doi:10.1029/2002JC001511.
- de Boyer Montégut, C., J. Vialard, S. S. C. Shenoi, D. Shankar, F. Durand, C. Ethe, and G. Madec (2007), Simulated seasonal and interannual variability of mixed layer heat budget in the northern Indian Ocean, *J. Clim.*, *20*, 3249–3268, doi:10.1175/JCLI4148.1.
- Du Penhoat, Y., and A.-M. Treguier (1985), The seasonal linear response of the Atlantic Ocean, *J. Phys. Oceanogr.*, *15*, 316–329, doi:10.1175/1520-0485(1985)015<0316:TSLROT>2.0.CO;2.
- Florenchie, P., J. R. E. Lutjeharms, C. J. C. Reason, S. Masson, and M. Rouault (2003), The source of Benguela Niños in the South Atlantic Ocean, *Geophys. Res. Lett.*, *30*(10), 1505, doi:10.1029/2003GL017172.
- Fraedrich, K., J. L. McBride, W. M. Frank, and R. Wang (1997), Extended EOF analysis of tropical disturbances: TOGA COARE, *J. Atmos. Sci.*, *54*(19), 2363–2372, doi:10.1175/1520-0469(1997)054<2363:EEAOTD>2.0.CO;2.
- França, C., I. Wainer, A. R. De Mesquita, and G. J. Goni (2003), Planetary equatorial trapped waves in the Atlantic Ocean from TOPEX/POSEIDON altimetry, in *Interhemispheric Water Exchange in the Atlantic Ocean*, Elsevier Oceanogr. Ser., vol. 68, edited by G. J. Goni and P. Malanotte-Rizzoli, pp. 213–232, Elsevier, New York.
- Gill, A. E. (1982), *Atmosphere–Ocean Dynamics*, 662 pp., Academic, New York.
- Greatbatch, R. J., and K. A. Peterson (1996), Interdecadal variability and oceanic thermohaline adjustment, *J. Geophys. Res.*, *101*, 20,467–20,482, doi:10.1029/96JC01531.
- Grodsky, S. A., and J. A. Carton (2006), Influence of the tropics on the climate of the South Atlantic, *Geophys. Res. Lett.*, *33*, L06719, doi:10.1029/2005GL025153.
- Guiavarc'h, C., A. M. Treguier, and A. Vangriesheim (2008), Remotely forced biweekly deep oscillations on the continental slope of the Gulf of Guinea, *J. Geophys. Res.*, *113*, C06002, doi:10.1029/2007JC004471.
- Han, W., P. J. Webster, J. Lin, W. T. Liu, R. Fu, D. Yuan, and A. Hu (2008), Dynamics of intraseasonal sea level and thermocline variability in the equatorial Atlantic during 2002–2003, *J. Phys. Oceanogr.*, *38*, 945–967.
- Handoh, I. C., and G. R. Bigg (2000), A self-sustaining climate mode in the tropical Atlantic, 1995–97: Observations and modelling, *Q. J. R. Meteorol. Soc.*, *126*, 807–821, doi:10.1256/smsqj.56402.
- Hendon, H. H., B. Liebmann, and J. D. Glick (1998), Oceanic Kelvin waves and the Madden-Julian Oscillation, *J. Atmos. Sci.*, *55*, 88–101, doi:10.1175/1520-0469(1998)055<0088:OKWATM>2.0.CO;2.
- Hill, K. L., I. S. Robinson, and P. Cipollini (2000), Propagation characteristics of extratropical planetary waves observed in the ATSR global sea surface temperature record, *J. Geophys. Res.*, *105*, 21,927–21,945, doi:10.1029/2000JC900067.
- Hormazabal, S., G. Shaffer, and O. Pizarro (2002), Tropical Pacific control of intraseasonal oscillations off Chile by way of oceanic and atmospheric pathways, *Geophys. Res. Lett.*, *29*(6), 1081, doi:10.1029/2001GL013481.
- Illig, S., B. Dewitte, N. Ayoub, Y. du Penhoat, G. Reverdin, P. De Mey, F. Bonjean, and G. S. Lagerloef (2004), Interannual long equatorial waves in the tropical Atlantic from a high-resolution ocean general circulation model experiment in 1981–2000, *J. Geophys. Res.*, *109*, C02022, doi:10.1029/2003JC001771.
- Illig, S., D. Gushchina, B. Dewitte, N. Ayoub, and Y. du Penhoat (2006), The 1996 equatorial Atlantic warm event: Origin and mechanisms, *Geophys. Res. Lett.*, *33*, L09701, doi:10.1029/2005GL025632.
- Jacobs, G. A., H. E. Hurlburt, J. C. Kindle, E. J. Metzger, J. L. Mitchell, W. J. Teague, and A. J. Wallcraft (1994), Decade-scale trans-Pacific propagation and warming effects of an El Niño anomaly, *Nature*, *370*, 360–363, doi:10.1038/370360a0.

- Kalnay, E., et al. (1996), The NCEP/NCAR 40-year reanalysis project, *Bull. Am. Meteorol. Soc.*, *77*, 437–471, doi:10.1175/1520-0477(1996)077<0437:TNYRPP>2.0.CO;2.
- Katz, E. J. (1997), Waves along the equator in the Atlantic, *J. Phys. Oceanogr.*, *27*, 2536–2544, doi:10.1175/1520-0485(1997)027<2536:WATEIT>2.0.CO;2.
- Kessler, W. S., M. J. McPhaden, and K. M. Weickmann (1995), Forcing of intraseasonal Kelvin waves in the equatorial Pacific, *J. Geophys. Res.*, *100*, 10,613–10,631, doi:10.1029/95JC00382.
- Levitus, S. (1998), Climatological atlas of the world ocean, *Tech. Rep. 13*, NOAA, Rockville, Md.
- Madec, G., P. Delecluse, M. Imbard, and C. Lévy (1998), OPA 8.1 ocean general circulation model reference manual, *Note Pole Model. 11*, 91 pp., Inst. Pierre-Simon Laplace, Paris.
- Matsuno, T. (1966), Quasi-geostrophic motions in the equatorial area, *J. Meteorol. Soc. Jpn.*, *44*, 25–43.
- Mayer, D. A., R. L. Molinari, M. O. Baringer, and G. J. Goni (2001), Transition regions and their role in the relationship between sea surface height and subsurface temperature structure in the Atlantic Ocean, *Geophys. Res. Lett.*, *28*, 3943–3946, doi:10.1029/2001GL013331.
- Meyers, S. D., A. Melsom, G. T. Mitchum, and J. O'Brien (1998), Detection of the fast Kelvin wave teleconnection due to El Niño–Southern Oscillation, *J. Geophys. Res.*, *103*, 27,655–27,663, doi:10.1029/98JC02402.
- Mittelstaedt, E. (1991), The ocean boundary along the northwest African coast: Circulation and oceanographic properties at the sea surface, *Prog. Oceanogr.*, *26*, 307–355, doi:10.1016/0079-6611(91)90011-A.
- Moore, D. W. (1968), Planetary-gravity waves in an equatorial ocean, Ph.D. thesis, Harvard Univ., Cambridge, Mass.
- Moore, D. W., P. Hisard, J. P. McCreary, J. Merle, J. J. O'Brien, J. Picaut, J. Verstraete, and C. Wunsch (1978), Equatorial adjustment in the eastern Atlantic, *Geophys. Res. Lett.*, *5*, 637–640, doi:10.1029/GL005i008p00637.
- O'Brien, J. J., D. Adamec, and D. W. Moore (1978), A simple model of upwelling in the Gulf of Guinea, *Geophys. Res. Lett.*, *5*, 641–644, doi:10.1029/GL005i008p00641.
- Philander, S. G. H. (1990), *El Niño, La Niña, and the Southern Oscillation*, *Int. Geophys. Ser.*, vol. 46, 293 pp., Academic, New York.
- Picaut, J. (1983), Propagation of the seasonal upwelling in the eastern equatorial Atlantic, *J. Phys. Oceanogr.*, *13*, 18–37, doi:10.1175/1520-0485(1983)013<0018:POTSUI>2.0.CO;2.
- Polito, P. S., and P. Cornillon (1997), Long baroclinic Rossby waves detected by TOPEX/POSEIDON, *J. Geophys. Res.*, *102*, 3215–3235, doi:10.1029/96JC03349.
- Rebert, J., J. Donguy, G. Eldin, and K. Wyrki (1985), Relations between sea level, thermocline depth, heat content, and dynamic height in the tropical Pacific Ocean, *J. Geophys. Res.*, *90*, 11,719–11,725, doi:10.1029/JC090iC06p11719.
- Rodriguez-Fonseca, B., I. Polo, E. Serrano, and M. Castro (2006), Evaluation of the north Atlantic SST forcing on the European and northern African winter climate, *Int. J. Climatol.*, *26*, 179–191, doi:10.1002/joc.1234.
- Rouault, M., S. Illig, C. Bartholomae, C. J. C. Reason, and A. Bentamy (2007), Propagation and origin of warm anomalies in the Angola Benguela upwelling system in 2001, *J. Mar. Syst.*, *68*, doi:10.1016/j.jmarsys.2006.11.010.
- Roundy, P. E., and G. N. Kiladis (2006), Observed relationships between oceanic Kelvin waves and atmospheric forcing, *J. Clim.*, *19*, 5253–5271, doi:10.1175/JCLI3893.1.
- Saravanan, R., and P. Chang (2000), Interaction between tropical Atlantic variability and El Niño–Southern Oscillation, *J. Clim.*, *13*, 2177–2194, doi:10.1175/1520-0442(2000)013<2177:IBTAVA>2.0.CO;2.
- Schouten, M. W., R. P. Matano, and T. P. Strub (2005), A description of the seasonal cycle of the equatorial Atlantic from altimeter data, *Deep Sea Res., Part 1*, *52*, 477–493, doi:10.1016/j.dsr.2004.10.007.
- Servain, J., J. Picaut, and J. Merle (1982), Evidence of remote forcing in the equatorial Atlantic Ocean, *J. Phys. Oceanogr.*, *12*, 457–463, doi:10.1175/1520-0485(1982)012<0457:EORFIT>2.0.CO;2.
- Stammer, D. (1997), Global characteristics of ocean variability estimated from regional TOPEX/POSEIDON altimeter measurements, *J. Phys. Oceanogr.*, *27*, 1743–1769, doi:10.1175/1520-0485(1997)027<1743:GCOOVE>2.0.CO;2.
- Sutton, R. T., S. P. Jewson, and D. P. Rowell (2000), The elements of climate variability in the tropical Atlantic region, *J. Clim.*, *13*, 3261–3284, doi:10.1175/1520-0442(2000)013<3261:TEOCVI>2.0.CO;2.
- Trenberth, K. E., J. G. Olson, and W. G. Large (1989), A global ocean wind stress climatology based on the ECMWF analyses, *NCAR Tech. Note TN-338+STR*, 93 pp., Natl. Cent. for Atmos. Res., Boulder, Colo.
- UNESCO, (1996), *Discharge of Selected Rivers of the World*, vol. II (part II), Paris.
- Vega, A., Y. Du-Penhoat, B. Dewitte, and O. Pizarro (2003), Equatorial forcing of interannual Rossby waves in the eastern South Pacific, *Geophys. Res. Lett.*, *30*(5), 1197, doi:10.1029/2002GL015886.
- Weare, B. C., and J. S. Nasstrom (1982), Examples of extended empirical orthogonal function analysis, *Mon. Weather Rev.*, *110*, 481–485, doi:10.1175/1520-0493(1982)110<0481:EOEOF>2.0.CO;2.
- Wilson, C., and D. Adamec (2002), A global view of bio-physical coupling from SeaWiFS and TOPEX satellite data, 1997–2001, *Geophys. Res. Lett.*, *29*(8), 1257, doi:10.1029/2001GL014063.
- Xie, P., and P. A. Arkin (1996), Analysis of global monthly precipitation using gauge observations, satellite estimates and numerical model predictions, *J. Clim.*, *9*, 840–858, doi:10.1175/1520-0442(1996)009<0840:AOGMPU>2.0.CO;2.

S. Arnault and A. Lazar, LOCEAN-IPSL, University of Paris VI, 4 place jussieu, F-75252 Paris CEDEX 05, France.

I. Polo and B. Rodriguez-Fonseca, Departamento de Geofísica y Meteorología, Facultad de C.C. Físicas, Universidad Complutense Madrid, Avenue Complutense, E-28040 Madrid, Spain. (ipolo@fis.ucm.es)